



## Full length article

# The anisotropy of deformation twinning in bcc materials: Mechanical loading, temperature effect, and twin–twin interaction

Amir Hassan Zahiri <sup>a,1</sup>, Mehrab Lotfpour <sup>a,1</sup>, Jamie Ombogo <sup>a</sup>, Eduardo Vitral <sup>b</sup>, Lei Cao <sup>a,\*</sup><sup>a</sup> Department of Mechanical Engineering, University of Nevada, Reno, Reno, NV, 89557, USA<sup>b</sup> Department of Mechanical Engineering, Rose-Hulman Institute of Technology, Terre Haute, IN, 47803, USA

## ARTICLE INFO

**Keywords:**

Twinning  
Tension–compression asymmetry  
Temperature effect  
Martensitic phase transformation  
Molecular dynamics simulations

## ABSTRACT

By integrating atomistic simulations with theoretical calculations, we investigate the prevalence of  $\{112\}$  deformation twins in bcc materials and their sensitivity to the loading direction as well as temperature. Our atomistic simulations reveal the copious occurrence of  $\{112\}$  twins involving either hcp or fcc intermediate phases. The hcp and fcc cases occur in bcc titanium alloy during [100] compression and tension, respectively. Similarly, they can also manifest in bcc iron under different temperature conditions. Furthermore, by calculating the correspondence matrix, we identify the fcc and hcp cases as the normal deformation twin mode and the 1/2 atoms-shuffle mode, respectively. The twinning modes have a significant influence on twin–twin interactions and the final microstructure. Our theoretical calculation confirms that the selection of specific twin modes and twin variants is governed by the correlation between their deformation path and mechanical loading. The results underscore the crucial role of mechanical loading and temperature in activating the specific twin modes, thereby providing a novel avenue for engineering twin microstructures through carefully designed thermomechanical processing techniques.

## 1. Introduction

Plastic deformation of body-centered cubic (bcc) metals at room temperature and moderate strain rates is limited by the slip of screw dislocations [1–6]. These dislocations have low mobility due to their non-planar dislocation core and high lattice resistance, limiting the ductility of bcc metals [2,7,8]. One effective approach to enhancing ductility is by activating additional deformation mechanisms alongside dislocation slip. For instance, in recently developed metastable titanium (Ti) alloys, the high ductility is attributed to transformation-induced and twinning-induced plasticity, the latter of which is achieved through the  $\{332\}$  twin mode in addition to the conventional  $\{112\}$  twin mode [9,10]. Recent studies have demonstrated twinning as an additional deformation mechanism in bcc metals through in-situ transmission electron microscopy investigations of nanoscale deformation [11–13]. Notably, Wang et al. [14] conducted in-situ nanomechanical testing and observed the superior plastic deformation in bcc niobium (Nb) nanowires. The remarkable superplasticity is attributed to the simultaneous activation of three distinct mechanisms—stress-induced phase transformation, deformation twinning, and slip-induced crystal rotation. In another study of bcc tungsten, most deformation twins exhibited instability and underwent detwinning upon unloading [15],

contrary to the notion that twinning represents a permanent plastic deformation [16]. The instability of bcc twins was found to be proportional to the fraction of inclined twin boundaries that deviate from the  $\{112\}$  habit plane. These studies affirm the significant potential for inducing deformation twinning in bcc materials. Though still in the early stages, further research is required to gain a deeper understanding of twinning mechanisms in bcc materials [11].

Some recent studies emphasized the correlation between twinning and phase transformation, and proposed transformation-assisted twinning mechanisms [11,17–26]. Notably, Li et al. [27] proposed three types of phase transformation mediated twinning pathways, rooted in the experimental observation of metastable interfacial phases ( $\omega$  or orthorhombic) at the twin boundaries in bcc metals or alloys [27–32]. On the other hand, Gao et al. [20] conducted a theoretical investigation into the relationship between symmetry breaking during phase transformation and deformation twinning in bcc structures. They proposed that along the deformation path of bcc twins there exist intermediate high symmetry states, including face-centered cubic (fcc), hexagonal close-packed (hcp),  $\omega$ , and orthorhombic states. Importantly, they proposed that different twinning modes correspond to the topological defects arising from the symmetry breaking in different intermediate

\* Corresponding author.

E-mail address: [leicao@unr.edu](mailto:leicao@unr.edu) (L. Cao).<sup>1</sup> Equal contribution.

high symmetry states. In another study by Yang et al. [33], molecular dynamic (MD) simulations were employed to investigate the phase transformations and twinning behavior in nanoscale iron (Fe) with different carbon contents. Their findings demonstrated that when the fcc structure was stretched along the [100] direction, it underwent the fcc–bcc phase transformation, concurrently resulting in the formation of {112} twins between neighboring bcc grains.

Unlike dislocation slip, twinning shear exclusively occurs in a unidirectional manner, and merely reversing the shear direction does not lead to the same twin relation. Therefore, the loading directions have the potential to impact twin formation in various crystal structures [34]. In hcp materials, it is well-known that deformation twinning exhibits a tension–compression asymmetry. When the *c*-axis of the hcp structure is subjected to compression, {10̄11} and {11̄22} twins are activated, whereas under tension, {10̄12} and {11̄21} twins come into play [17,35–37]. Though twinning modes asymmetry has not been explored in bcc structure, numerous bcc metals demonstrate a twinning–antitwinning asymmetry in terms of slip resistance. Shearing the crystal in the twinning direction leads to the easier glide of dislocations and the initiation of twin embryos. Conversely, when shearing the crystal in the opposite (antitwinning) direction, significantly greater resistance is encountered. [1,38,38–42]. The direct observation of twinning in the antitwinning direction was not available until a very recent study. Wang et al. [41] employed in-situ transmission electron microscopy to investigate the deformation of nanoscale bcc tungsten. This study revealed that the nucleation and growth of antitwinning require ultrahigh stresses, a condition made feasible by the nanoscale deformation.

Temperature is another crucial parameter that can profoundly influence the activation of various twinning modes. For instance, in hcp zirconium, it was found that the {10̄11} contraction twin occurred at lower temperatures, the {11̄22} contraction twin was favored at higher temperatures, while the {10̄12} tension twin was formed consistently across a wide range of temperatures [43,44]. Similarly, during the compression of polycrystalline titanium, {11̄22} twins were present from room temperature up to 673 K, while the {10̄11} twin predominated at temperatures above 673 K [45]. In bcc materials, the temperature effect was mostly focused on the twinning–dislocation transition. Although the influence of temperature on the activation of different twinning modes in bcc structures remains relatively unexplored, it is reasonable to expect similar temperature-dependent variations.

In this study, we aim to investigate the influence of mechanical loading and temperature on twinning behavior in bcc materials. As such, we focused on two representative bcc materials: pure Fe and a bcc Ti–Nb alloy. Fe is a widely used structural metal that exists in the bcc structure at ambient conditions. When exposed to elevated temperature or high-pressure conditions, it undergoes transformations into fcc or hcp structures, respectively [46]. Metastable bcc Ti alloys have wide applications in various industries such as biomedical, automotive, and aerospace, due to their excellent biocompatibility, corrosion resistance, and fatigue strength. While pure Ti has an hcp structure at room temperature, the addition of Nb stabilizes Ti–Nb alloys into the bcc structure [47]. When subjected to tension and compression along various directions, these bcc structures consistently form {112} twins, albeit through distinct mechanisms that involve either hcp or fcc intermediate phases. In order to investigate the mechanisms underlying twin formation, we conduct extensive analysis and theoretical calculations. This comprehensive examination illuminates the pivotal factors influencing twinning behavior within bcc structures.

This paper is organized as follows. Section 2 describes the methods for the MD simulations. Section 3 shows the MD simulations in single-crystal Ti–Nb and polycrystal Fe, followed by the theoretical calculation of variant selection and twinning modes for different {112} twins. Finally, conclusions are presented in Section 4.

## 2. Methods

The MD simulations are performed using the LAMMPS package [48], with a time-step size of 1 fs. To avoid any artificial free surface effects, periodic boundary conditions are applied in all three dimensions. Initially, the atoms are initialized with random velocities drawn from a Gaussian distribution, corresponding to an average temperature of 10 K. Subsequently, a relaxation of 100 ps is carried out at 10 K and 0 Pa utilizing the Nosé–Hoover thermostat [49] and the Parrinello–Rahman barostat [50] and within the isothermal–isobaric ensemble. To ensure a clear visualization of the microstructure evolution [17,51] and minimize thermal fluctuations, the deformation is simulated at a low temperature of 10 K. The crystalline structures are identified using the common neighbor analysis [52,53] in OVITO [54], where the bcc, hcp, fcc, and amorphous phases are denoted by the colors red, blue, green, and yellow, respectively. Extensive simulations are conducted across a range of strain rates, from  $10^8$  to  $10^{10}$  s $^{-1}$ . It is observed that the key twinning behavior remains consistent regardless of the applied strain rate.

This study investigates two systems: a single-crystal Ti-10 at.%Nb and a polycrystalline Fe. Metastable Ti alloys exhibit diverse twinning modes ({112}, {332}, {5 8 11}, {10 9 3} twins) in room-temperature experiments [55,56]. Therefore, we selected the Ti–Nb alloy to investigate and demonstrate tension–compression asymmetry in the twinning process. Strain rates in MD simulations are much higher than those used in experiments, so loading has a predominant effect on deformation compared to temperature, which is a secondary factor in most scenarios of MD simulations. This does not pose a challenge to observe temperature asymmetry in Fe because it has a well-known high-temperature fcc phase and a high-pressure low-temperature hcp phase. Additionally, the intentional choice of polycrystalline Fe over a single crystal aligns more closely with realistic structures used in experiments and real-world applications. Considering all the factors discussed above, our research utilizes Ti–Nb as the model system to illustrate loading asymmetry and Fe as the model system to explore temperature asymmetry. The Ti–Nb single-crystal consists of one million atoms and has dimensions of  $29.5 \times 25.5 \times 24$  nm $^3$  along the [100], [011], and [0̄11] directions. Within the matrix of Ti atoms, the Nb atoms are randomly distributed in substitutional positions. To model the interactions between Nb and Ti atoms, the modified embedded-atom method potential developed by Huang et al. [57] is employed. This potential has been specifically designed to accurately predict phase transformations and mechanical properties in TaHfNbTiZr high entropy alloys, thus making it suitable for the Ti–Nb system.

The polycrystalline Fe has dimensions of  $27.5 \times 27.5 \times 23.7$  nm $^3$  and consists of one million Fe atoms. The creation of the Fe polycrystal involves utilizing a template from our previous study [34]. Subsequently, the polycrystal undergoes a full relaxation using the modified embedded-atom method potential developed by Etesami et al. [58]. The relaxation is carried out at 10 K and 0 Pa within the isothermal–isobaric ensemble, employing the Nosé–Hoover thermostat [49] and the Parrinello–Rahman barostat [50] for a duration of 100 ps. The deformation is subsequently applied at strain rates of  $10^9$  and  $10^{10}$  s $^{-1}$ , and under temperatures of 10 K and 800 K.

## 3. Results

This section presents the effects of the loading direction and temperature on the twinning behavior in both single-crystal and polycrystalline bcc structures. In the single-crystal bcc Ti–Nb alloy, MD simulations are performed to study the influence of loading direction on twin formation. The choice of a single crystal facilitates a more straightforward theoretical analysis, enabling a comprehensive examination of variant selection, twinning modes, and twin–twin interactions. In the polycrystalline bcc Fe, MD simulations are conducted to investigate the temperature effect on twinning behavior.

### 3.1. The effect of loading direction

#### 3.1.1. Tension–compression asymmetry

To investigate the deformation of Ti–Nb single crystal, we conduct MD simulations under six different loading conditions, including uniaxial tension and compression along the  $x$  ([100]),  $y$  ([011]), or  $z$  ([0̄11]) axes. As shown in Fig. 1, tension–compression asymmetry is observed in simulations across all the strain rates ( $10^8$  to  $10^{10}$  s $^{-1}$ ) and for various loading conditions. For instance, when subjected to [100] loading, the single crystal demonstrates a yield strength of 13 GPa at approximately 13% strain during compression, whereas it yields at 8 GPa with an 8% strain level during tension (Fig. 1a). This yielding disparity is attributed to the significantly higher resistance in the antitwinning direction compared to the twinning direction [35,38–41]. Specifically, the applied tension along [100] produces a shear stress in the twinning sense, whereas the compression induces a shear in the antitwinning sense. Due to Poisson’s effect, tension–compression asymmetry exhibits an opposite trend under [011] loading when compared to [100] loading. As depicted in Fig. 1b, the crystal yields earlier in compression than in tension. Furthermore, this tension–compression asymmetry remains consistent when loading along [011] or [0̄11] axes, as these directions belong to the same crystallographic family.

It is found that the stress–strain curves and the underlying microstructure evolution are consistent for all strain rates. Therefore, we will present our detailed analysis for the case with a strain rate of  $10^{10}$  s $^{-1}$ . This choice is further motivated by the prevalence of deformation twins and the intriguing presence of intermediate phases under a higher strain rate. Fig. 2 shows the microstructure evolution under uniaxial compression along the [100] direction. The top row presents the projection along [011] direction, while the bottom row shows the projection along [0̄11] direction. As depicted in Fig. 2b, a significant number of local bcc-hcp phase transformations occur when the strain reaches 13.72%. When the strain is further increased to 14.60%, a few hcp regions undergo a transformation back to a new bcc phase that exhibits a different orientation from the parent bcc phase (Fig. 2c). At a strain of 18.00%, the majority of hcp regions have transformed back into the bcc phase (Fig. 2d). Notably, the newly formed bcc phase exhibits a misorientation angle of 70.53° degrees around the [011] axis with respect to the parent bcc phase, resulting in a {112} twin relationship.

The final microstructure exhibits the activation of multiple twin variants. In Fig. 2h, two co-zone twin variants (bcc1 and bcc2) can be observed in the projection along [0̄11]. Similarly, two other co-zone twin variants (bcc3 and bcc4) are identified in the projection along [011] (Fig. 2d). Due to different common zone axes, variants bcc1 and bcc2 are non-co-zone with variants bcc3 and bcc4. In Fig. 2e, we provide a schematic representation of the four twin variants observed in the MD simulation of [100]-compression.

The loading of [011] or [0̄11]-tension also results in a shear stress in the antitwinning direction. We observe a consistent microstructure evolution, and therefore, only present the case of [011]-tension for illustration. Similar to the case of [100]-compression, the formation of the intermediate hcp phase and {112} twins are observed in the projection along [0̄11] (bottom row in Fig. 3). Interestingly, no twinning is observed in the projection along [011] this time (top row in Fig. 3). As schematically illustrated in Fig. 3e, two co-zone twin variants (bcc1 and bcc2) are formed, both of which possess a common zone axis along [0̄11].

In contrast, the microstructure evolution under [100]-tension exhibits a distinct pattern compared to that formed under compressive loading. Notably, a fcc intermediate phase is formed under tension (Fig. 4b), in contrast to the hcp intermediate phase formed under compression (Fig. 2b). Specifically, numerous slender and elongated {112} nuclei are observed at a strain of 10.00% (Fig. 4f). Thin layers of fcc atoms are present within the twin nuclei and two equivalent twin variants appear simultaneously. Upon reaching a strain of 12.00%,

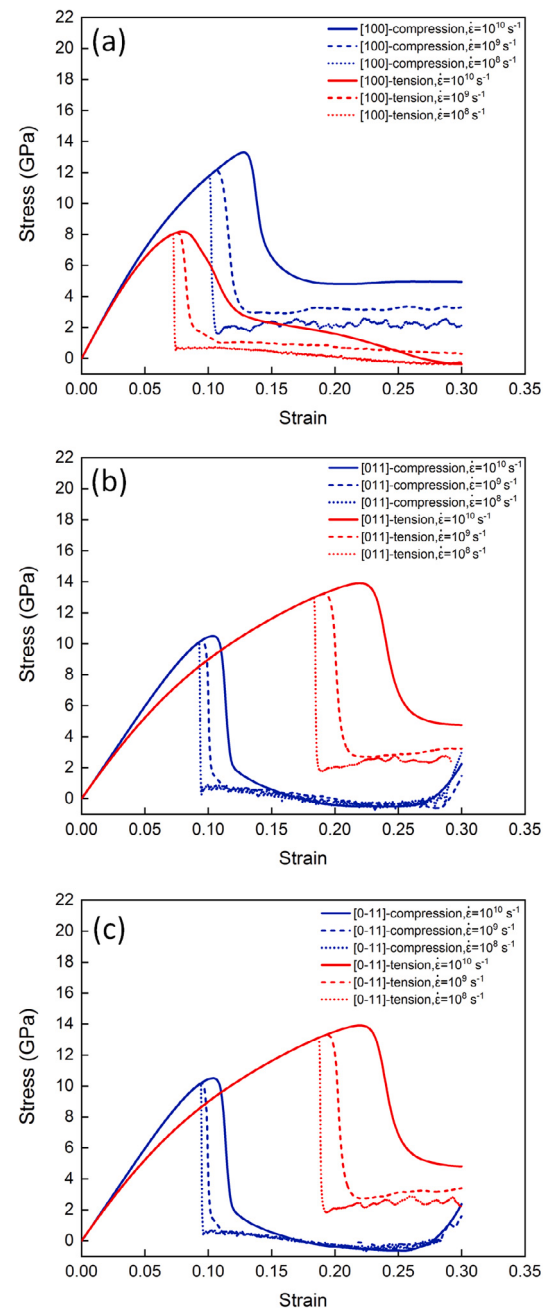


**Fig. 1.** Stress–strain curves of single-crystal Ti–Nb under tensile (red) and compressive (blue) loading, obtained from the MD simulations at 10 K and strain rates of  $10^8 \sim 10^{10}$  s $^{-1}$ . (a) Along [100] loading, compression exhibits a higher yield strength than tension. Conversely, when loading along (b) [011] or (c) [0̄11] directions, tension demonstrates a higher yield strength compared to compression. (For interpretation of the references to color in this figure legend, the reader is referred to the web version of this article.)

the fcc layers within the {112} twin nuclei transform into twin bcc phases, completing the twin nucleation process (Fig. 4g). As deformation progresses, the twin boundaries propagate significantly and the {112} twins continue to grow, leading to significant coherent twin boundaries. Finally, at a strain of 22.00%, the merging of the two {112} twin variants can be observed at numerous impinging twin tips (Fig. 4h). Meanwhile, two additional {112} twin variants are initially observed in the projection along [011] direction (Fig. 4b and c), which subsequently undergo detwinning in some regions (Fig. 4d). As illustrated in Fig. 4e, four variants (bcc1, bcc2, bcc3, bcc4) are observed

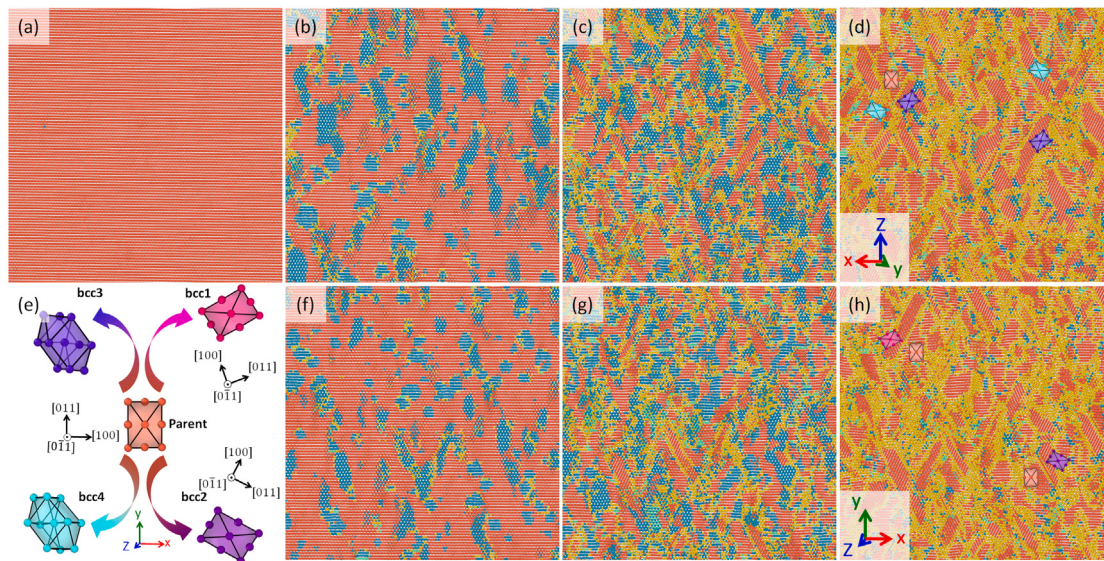


**Fig. 2.** Microstructure evolution in a Ti–Nb single crystal under [100]-compression at the strain rate of  $10^{10}$  s $^{-1}$  and the temperature of 10 K. The top row presents the microstructure projected along [011] direction, while the bottom row shows the projection along [0-11] direction. (a) The initial state features of the bcc single-crystal. (b) Nucleation of the hcp phase occurs in various regions at a strain of 13.27%. (c) A few {112} twins form after the reverse hcp-bcc phase transformation. (d) Most hcp regions are eliminated as a result of the reverse phase transformation at a strain of 18.00%. (f-h) The microstructure evolution in the projection along the [0-11] direction exhibits a similar pattern. (e) A schematic depicting the four twin variants. The bcc, hcp, fcc, and amorphous phases are depicted in colors red, blue, green, and yellow, respectively. (For interpretation of the references to color in this figure legend, the reader is referred to the web version of this article.)

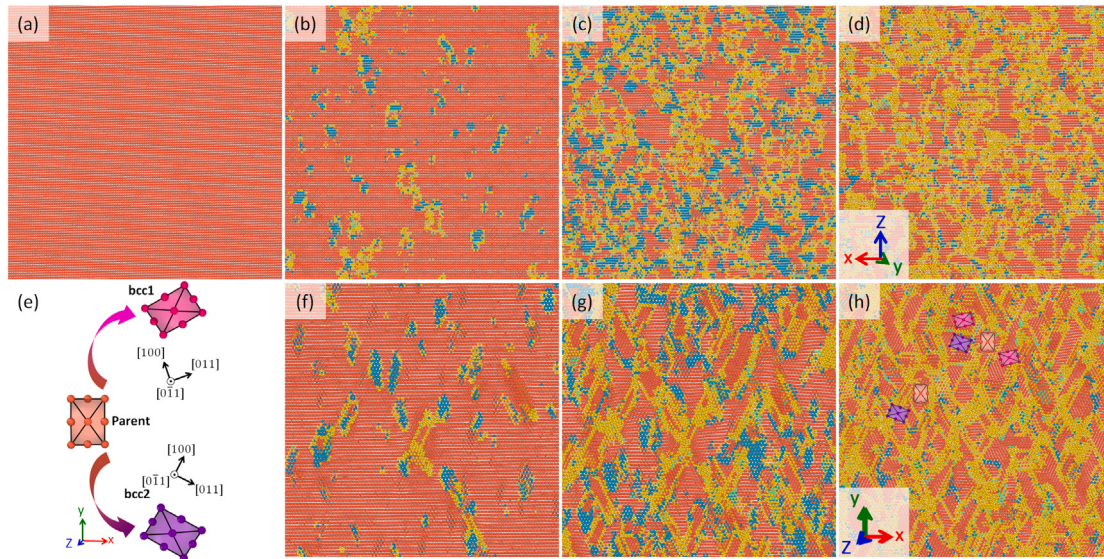


**Fig. 3.** Microstructure evolution in the Ti–Nb single crystal under [011]-tension at the strain rate of  $10^{10}$  s $^{-1}$  and the temperature of 10 K. The top row presents the microstructure projected along [011] direction, while the bottom row shows the projection along [0-11] direction. (a) The initial state features of the bcc single-crystal. (b)-(d) No twinning happens in the projection along [011]. (e) A schematic depicting the two twin variants. The bcc, hcp, fcc, and amorphous phases are depicted in colors red, blue, green, and yellow, respectively. (f-h) The microstructure evolution in the projection along the [0-11] direction exhibits a similar pattern. (e) A schematic depicting the two twin variants. The bcc, hcp, fcc, and amorphous phases are depicted in colors red, blue, green, and yellow, respectively. (For interpretation of the references to color in this figure legend, the reader is referred to the web version of this article.)

in the case of [100]-axis tension. However, bcc3 and bcc4 grow less compared to bcc1 and bcc2.

A compressive load in the [011] or [0-11] directions also induces shear stress in the twinning direction. In Fig. 5, we only present the microstructure evolution for the [011]-compression case, as both loading scenarios exhibit a consistent evolution pattern. Similar to the [100]-tension case, the formation of the intermediate fcc phase and {112} twins are observed in the projection along [0-11] (Fig. 5h). However, no twinning is observed in the projection along [011] this time (Fig. 5d).

As schematically illustrated in Fig. 5e, two co-zone twin variants (bcc1 and bcc2) are formed, both of which possess a common zone axis along [011].

It should be noted that Poisson's effect induces different trends of tension–compression asymmetry depending on the loading axis. Nevertheless, the presence of intermediate phases is characteristic of a given deformation and offers an efficient way to differentiate between different simulations. For example, for [100] loading, we will use the terms “fcc case” or “hcp case” as shorthand to refer to [100]-tension

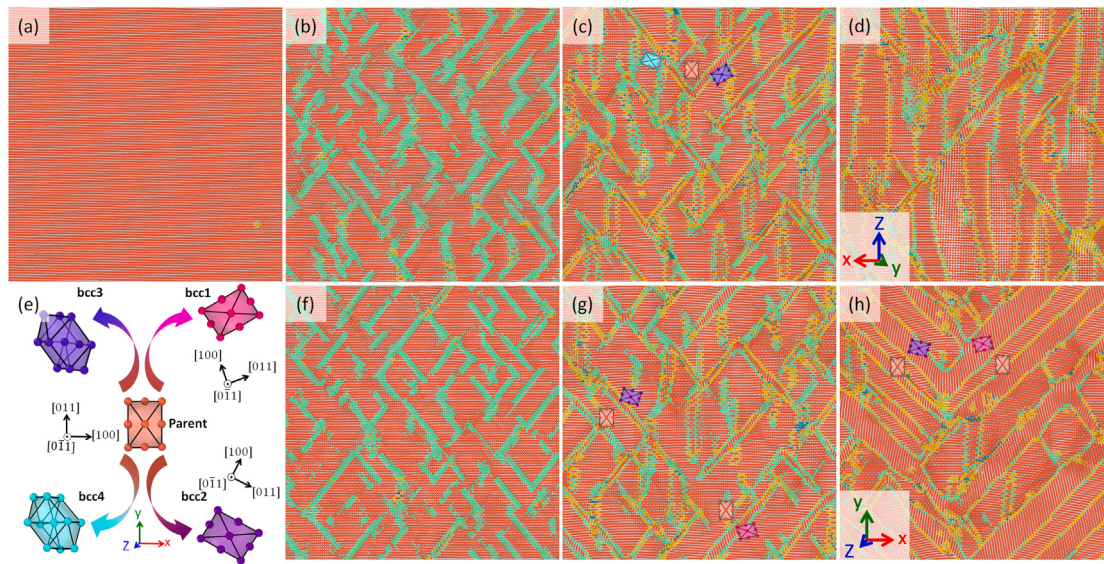


**Fig. 4.** Microstructure evolution in Ti-Nb single crystal under [100]-tension at a strain rate of  $10^{10}$  s $^{-1}$  and a temperature of 10 K. The top row presents the microstructure projected along [011] direction, while the bottom row shows the projection along [0̄11] direction. (a) The initial structure is a bcc single crystal. (f) {112} twin nuclei begin to form, accompanied by the presence of fcc atomic layers within. (g) Twins are formed completely when the fcc atoms inside the twin nuclei transform back to the bcc phase. (h) The rapid propagation and growth of two {112} twin variants. (b-c) Similar microstructure evolution is initially observed in the projection along [011] direction, with some local detwinning occurring at a strain of 22.00% in (d). (e) A schematic depicting the two twin variants. The red, blue, green, and yellow colors represent the bcc, hcp, fcc, and amorphous phases, respectively. (For interpretation of the references to color in this figure legend, the reader is referred to the web version of this article.)

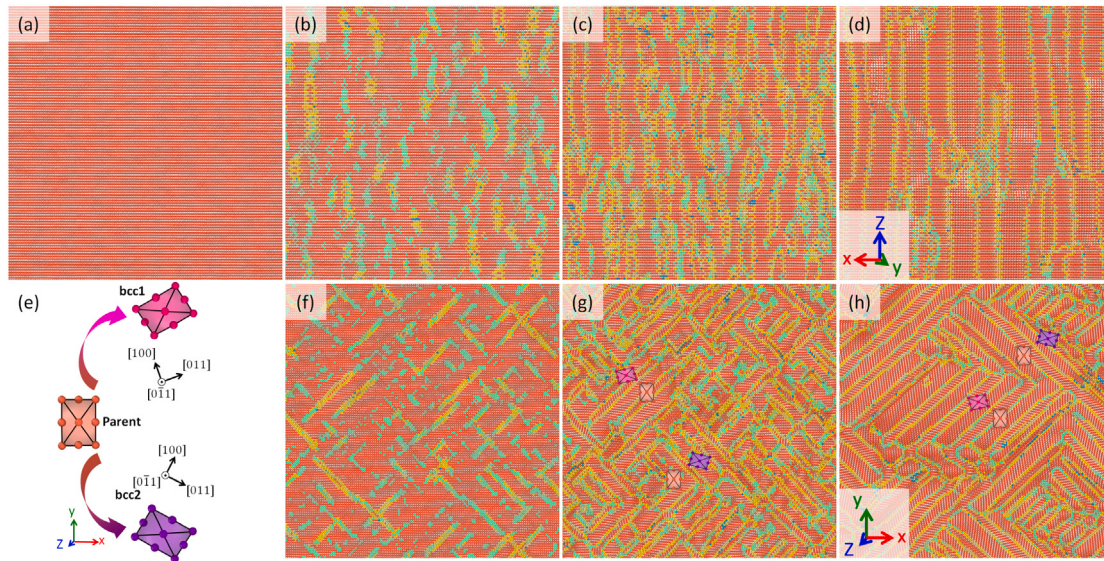


**Fig. 5.** Microstructure evolution in Ti-Nb single crystal under [011]-compression at a strain rate of  $10^{10}$  s $^{-1}$  and a temperature of 10 K. The top row presents the microstructure projected along [011] direction, while the bottom row shows the projection along [0̄11] direction. (a) The initial structure is a bcc single crystal. (f) {112} twin nuclei begin to form at the strain of 11.20%, accompanied by the presence of fcc atomic layers within. (g) Twins are formed completely when the fcc atoms inside the twin nuclei transform back to the bcc phase at the strain of 12.00%. (h) The rapid propagation and growth of two {112} twin variants at the strain of 18.00%. (b-d) No twinning is observed in the projection along [011]. (e) A schematic depicting the four twin variants. The red, blue, green, and yellow colors represent the bcc, hcp, fcc, and amorphous phases, respectively. (For interpretation of the references to color in this figure legend, the reader is referred to the web version of this article.)

or compression, respectively. Similarly, for [011] or [0̄11] loading, “fcc case” or “hcp case” are shorthand to denote compression or tension, respectively.

It is crucial to note that the deformation twinning observed in our simulations follows a two-step process: a bcc-to-intermediate phase transition followed by an intermediate-to-twin bcc phase transition. Such transformation-assisted twinning processes have been reported for both pure bcc metals and metastable Ti alloys [11,23–27]. Notably, twin nucleation commences from multiple locations without any preceding defects, such as dislocations or free surfaces. Therefore, we assert that this process is homogeneous twin nucleation, largely due

to the elevated strain rate inherent in MD simulations and the single crystal used in our work.

The nucleation, growth, and twin-twin interactions significantly influence the overall stress-strain response, which is thoroughly demonstrated in Fig. S1 of the supplementary materials. The yield point aligns with the initial activation of multiple local bcc-hcp or bcc-fcc phase transformations, i.e., the first step of the observed twinning process. Substantial stress drops are notable as the phase transformation progresses, ceasing upon the reverse transformation back to the twin bcc phase and the complete nucleation of twins. This behavior occurs in both twinning and antitwinning loading directions.

Following twin nucleation, the fcc case exhibits notable twin merging and fast twin growth, leading to a substantial additional stress drop. The twin growth is mediated by the nucleation and propagation of twinning dislocations along the coherent twin boundary. Eventually, the entire single crystal becomes nearly fully twinned, which is evident in the stress-strain curve, displaying an exceptionally low flow stress. Conversely, the hcp case exhibits significantly higher flow stress due to limited twin growth.

Again, we emphasize that the twinning process observed in our simulations shares fundamental similarities with the transformation-assisted twinning processes reported in the literature [23–26,30]. It is crucial to recognize the significant influence of the material system on the phase stability of the metastable intermediate phases. This variation in phase stability can result in twinning following distinct deformation paths, exemplified by the bcc-hcp-bcc twinning path in our work, as opposed to the bcc- $\omega$ -bcc twinning path in [27,30].

### 3.1.2. Variant selection

Interestingly, four twin variants are observed in loading along [100], while only two variants are observed in loading along [011] or [0̄1]. We will conduct theoretical calculations to quantitatively investigate the twin variant selection. The correspondence matrix  $C_{ij}$  is used to characterize the twinning deformation in the parent bcc lattice basis relative to the twin bcc lattice basis [35,59]. This matrix can be obtained from the components of a tensor  $C$ , in standard basis. It departs from the actual distortion by a rotation (change of basis), where the distortion is the deformation gradient of the lattice's displacive transformation. Generally, the distortion does not involve a significant rigid-body rotation, allowing it to be approximated by a stretch tensor through its polar decomposition. In this case, such stretch tensor coincides with the symmetric positive definite right stretch tensor  $U = \sqrt{C^T \cdot C}$ , obtained from the polar decomposition of  $C$ . The stretch tensor  $U$  is crucial for determining the favored twin variants under an applied load, and later on for solving the twinning equation to obtain the complete twinning components.

By denoting  $G_i$  and  $g_i$  as the parent and twin lattice bases, respectively, we can express  $C = g_i \otimes G^i$ , where  $G^i$  represents the reciprocal parent basis satisfying  $G_i \cdot G^j = \delta_i^j$ . These bases can be identified directly from the MD simulations. We will begin with the hcp case, where the twin variants remain stable and detwinning is not observed. From the MD simulations in Fig. 2, three orthogonal directions are tracked during the entire twinning process, as shown in Fig. 6. This monitoring yields one set of orientation relations, expressed as follows:

$$\begin{aligned} [100]_{bcc} &\leftrightarrow \frac{1}{3}[1\bar{1}20]_{hcp} \leftrightarrow \frac{1}{2}[1\bar{1}\bar{1}]_{bcc1} \\ [011]_{bcc} &\leftrightarrow [1\bar{1}00]_{hcp} \leftrightarrow \frac{1}{2}[311]_{bcc1} \\ [0\bar{1}1]_{bcc} &\leftrightarrow [0001]_{hcp} \leftrightarrow [0\bar{1}1]_{bcc1}. \end{aligned} \quad (1)$$

Based on this lattice correspondence, we define the parent basis as  $G_1 = a_0 e_1$ ,  $G_2 = a_0 (e_2 + e_3)$  and  $G_3 = a_0 (-e_2 + e_3)$ , while the twin basis as  $g_1 = (a_0/2)(e_1 - e_2 - e_3)$ ,  $g_2 = (a_0/2)(3e_1 + e_2 + e_3)$  and  $g_3 = a_0 (-e_2 + e_3)$ . The correspondence matrix  $C_{ij}$  calculated from these bases is

$$C_{ij}|_{bcc-hcp-bcc1} = \begin{bmatrix} 0.5 & 0.75 & 0.75 \\ -0.5 & 0.75 & -0.25 \\ -0.5 & -0.25 & 0.75 \end{bmatrix}. \quad (2)$$

Besides the variant bcc1 associated with the pathway in Eq. (2), its co-zone variant bcc2 has the correspondence matrix of

$$C_{ij}|_{bcc-hcp-bcc2} = \begin{bmatrix} 0.5 & -0.75 & -0.75 \\ 0.5 & 0.75 & -0.25 \\ 0.5 & -0.25 & 0.75 \end{bmatrix}. \quad (3)$$

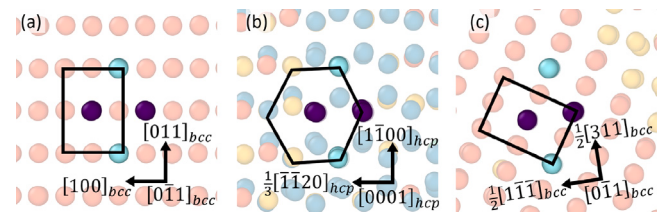


**Fig. 6.** Identification of lattice correspondence in the hcp case. (a) Two orthogonal directions are traced in the parent phase, with the purple and cyan atoms representing the  $[100]_{bcc}$  and  $[011]_{bcc}$  directions. (b) Following the bcc-hcp phase transformation, the two traced directions transformation into  $\frac{1}{3}[1\bar{1}20]_{hcp}$  and  $[1\bar{1}00]_{hcp}$ . (c) With the hcp-bcc transformation completing the twin formation process, the traced directions inside the twin evolve into  $\frac{1}{2}[1\bar{1}\bar{1}]_{bcc1}$  and  $\frac{1}{2}[311]_{bcc1}$ , respectively. (For interpretation of the references to color in this figure legend, the reader is referred to the web version of this article.)

**Table 1**

Biot strain component along three different crystalline directions for each of the twelve variants formed under the bcc-hcp-bcc path.

Variant	Biot strain		
	$[100]$ -direction	$[011]$ -direction	$[0\bar{1}1]$ -direction
bcc1	-0.1384	+0.3387	0
bcc2	-0.1384	+0.3387	0
bcc3	-0.1384	0	+0.3387
bcc4	-0.1384	0	+0.3387
bcc5	+0.0847	+0.0694	-0.1768
bcc6	+0.0847	-0.1768	+0.0694
bcc7	+0.0847	-0.1768	+0.0694
bcc8	+0.0847	+0.0694	-0.1768
bcc9	+0.0847	+0.0694	-0.1768
bcc10	+0.0847	-0.1768	+0.0694
bcc11	+0.0847	+0.0694	-0.1768
bcc12	+0.0847	-0.1768	+0.0694

For the twin variants bcc3 and bcc4, correspondence matrices read

$$C_{ij}|_{bcc-hcp-bcc3} = \begin{bmatrix} 0.5 & -0.75 & 0.75 \\ 0.5 & 0.75 & 0.25 \\ -0.5 & 0.25 & 0.75 \end{bmatrix}, \quad (4)$$

$$C_{ij}|_{bcc-hcp-bcc4} = \begin{bmatrix} 0.5 & 0.75 & -0.75 \\ -0.5 & 0.75 & 0.25 \\ 0.5 & 0.25 & 0.75 \end{bmatrix}.$$

It should be noted that the system can undergo twelve crystallographically equivalent bcc-hcp-bcc pathways based on the Burgers mechanism [20,60], in addition to the identity pathway [20]. However, the presence of a mechanical load introduces asymmetry to them, causing certain pathways to be favored over others. For an applied load along a specific direction ( $\mathbf{d}$ ), we determine the favored deformation path based on the Biot strain component  $e_d = (\mathbf{E}_{\text{Biot}} \cdot \mathbf{d}) \cdot \mathbf{d}$ , where the Biot strain tensor is related to the stretch tensor through  $\mathbf{E}_{\text{Biot}} = \mathbf{U} - \mathbf{I}$ . If  $e_d$  is greater than zero, the deformation path is favored under tension, whereas if  $e_d$  is smaller than zero, it is favored under compression.

As shown in Table 1, for [100]-compression, we find a favorable negative Biot strain  $e_d = (\mathbf{E}_{\text{Biot}} \cdot \mathbf{d}) \cdot \mathbf{d} = -0.1384$  for bcc1, bcc2, bcc3, and bcc4, with deformation pathways given in Eqs. (2), (3), and (4). On the other hand, the other eight non-identity pathways present a positive Biot strain and, therefore, are not favored by the compressive load.

As for [011]-tension, we find a favorable positive Biot strain  $e_d = (\mathbf{E}_{\text{Biot}} \cdot \mathbf{d}) \cdot \mathbf{d} = +0.3387$  for bcc1 and bcc2 with the deformation pathways represented by Eqs. (2) and (3). Four other variants also display a positive  $e_d$ , but the value is significantly smaller (+0.0694) than that for bcc1 and bcc2. Hence, the microstructure is expected to be populated by bcc1 and bcc2 under [011]-tension.

As for [0̄1]-tension, we find a favorable positive Biot strain  $e_d = (\mathbf{E}_{\text{Biot}} \cdot \mathbf{d}) \cdot \mathbf{d} = +0.3387$  for bcc3 and bcc4 with the deformation pathways represented by Eq. (4), besides four other variants presenting

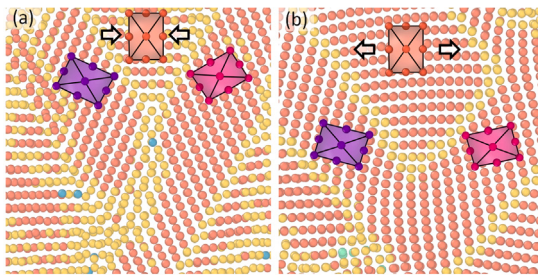


**Fig. 7.** The  $\{112\}$  twin-twin interactions in Ti–Nb single-crystal during (a) compression and (b) tension along the  $[100]$ -axis. The red unit cell represents the parent bcc, whereas the purple and pink unit cells correspond to two twin variants bcc1 and bcc2. The arrows indicate the loading directions. (For interpretation of the references to color in this figure legend, the reader is referred to the web version of this article.)

a significantly smaller  $e_d$  value (+0.0694). Using the same argument as in the previous case, the microstructure should be populated by bcc3 and bcc4 under  $[0\bar{1}1]$ -tension.

Similarly, the Biot strain analysis for the fcc cases also agrees with the variant selection observed in the MD simulations. As such, our theoretical calculations validate the variant selection in the MD simulations, confirming the number of variants and the specific variant to activate under the mechanical load. In other words, the twin variant selection here in single crystal Ti–Nb alloy is found to obey the Schmid law. Similarly, Bertrand et al. [61] confirmed that the activated variant has the highest Schmid factor in bcc Ti alloys. However, Min et al. [62] observed non-Schmid behavior for some primary and secondary twins in polycrystalline Ti–Mo–Zr alloys, which might be attributed to local stress variations in the polycrystals.

### 3.1.3. Twin–twin interactions

Among all the cases, detwinning is only observed in the case of  $[100]$ -tension. Our analysis reveals that the local detwinning is attributed to the unique twin–twin interactions. As different twin boundaries grow and approach each other, their interactions frequently result in the creation of intricate twin–twin boundaries, which show habit planes distinct from those of the original twins. For example, the interaction of two non-co-zone  $\{10\bar{1}2\}$  twin leads to the formation of a  $\{1\bar{1}\bar{2}2\}$  twin–twin boundary [51,63]. These twin–twin boundaries exist in such large quantities that they can even contribute to the emergence of a local misorientation peak in the electron backscatter diffraction misorientation histogram for both pure magnesium and its alloys [36,64].

In this work, we observe twin–twin interactions in both compressive and tensile loading, as shown in Fig. 7. Under  $[100]$ -compression (hcp case), two  $\{112\}$  twin variants form a twin relation characterized by a misorientation of  $51.1^\circ$  degrees across  $\langle 1\bar{1}0 \rangle$  (Fig. 7a). In contrast, during  $[100]$ -tension (fcc case), we observe the merging of the two twin variants and the formation of a single bcc variant (Fig. 7b). It is worth noting that the twin variants in both cases (the purple and pink bcc unit cells in Figs. 7 a and b) share the same orientation relative to the parent bcc structure. Surprisingly, they exhibit distinctly different twin–twin interactions. As such, we will solve the twining equation to quantitatively investigate the twin–twin interactions.

The twining equation is a kinematic compatibility condition that appears from the jump in the deformation gradient across a twin, whose solution has been discussed by Ball and James [65]. If a twin is formed between variants  $I$  and  $J$ , with right stretch tensors  $\mathbf{U}_I$  and  $\mathbf{U}_J$ , then the twining equation takes the form

$$\mathbf{Q} \cdot \mathbf{U}_I - \mathbf{U}_J = \mathbf{a} \otimes \mathbf{n}, \quad (5)$$

for some vector  $\mathbf{a}$  and a unit normal  $\mathbf{n}$  to the habit plane. The rotation tensor  $\mathbf{Q}$  contains information about the misorientation between

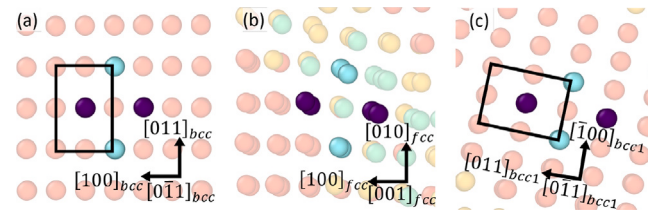


**Fig. 8.** Identification of lattice correspondence in the fcc case. (a) Two orthogonal directions are traced in the parent phase, with the purple and cyan atoms representing the  $[100]_{bcc}$  and  $[011]_{bcc}$  directions. (b) When the twin nucleus forms and exhibits the fcc structure, the two traced directions transform into  $[100]_{fcc}$  and  $[010]_{fcc}$ . (c) Upon the completion of twin formation, the traced directions inside the twin become  $[011]_{bcc1}$  and  $[100]_{bcc1}$ , respectively. (For interpretation of the references to color in this figure legend, the reader is referred to the web version of this article.)

the neighboring lattices. The procedure for calculating the twinning elements is detailed by Bhattacharya [66].

The direction of shear  $\boldsymbol{\eta}$ , habit plane  $\mathbf{K}$  and shear magnitude  $s$  can be calculated from the elements of (5) by

$$\boldsymbol{\eta} = \frac{\mathbf{a}}{|\mathbf{a}|}, \quad \mathbf{K} = \frac{\mathbf{U}_J^{-1} \cdot \mathbf{n}}{|\mathbf{U}_J^{-1} \cdot \mathbf{n}|}, \quad s = |\mathbf{a}| |\mathbf{U}_J^{-1} \cdot \mathbf{n}|. \quad (6)$$

When one of the variants is the reference lattice, say variant  $J$ , then  $\mathbf{U}_J = \mathbf{I}$ , which allows us to combine Eqs. (5) and (6) as follows

$$\mathbf{Q} \cdot \mathbf{U}_I - \mathbf{I} = s(\boldsymbol{\eta} \otimes \mathbf{K}). \quad (7)$$

Since the resulting deformation gradient for the twin bcc depends on the path the original bcc lattice undergoes, i.e., fcc or hcp-related path, so do the twinning elements from Eq. (7). We will start with the hcp case, for which the lattice correspondence has been derived in Eqs. (2), (3), and (4). For twin–twin interactions between bcc1 and bcc2, the stretch  $\mathbf{U}_I$  is calculated from the total correspondence  $\mathbf{C}_{bcc-hcp-bcc1} \cdot \mathbf{C}_{bcc-hcp-bcc2}^{-1}$ . Based on this stretch, from Eq. (7) we obtain

$$\begin{aligned} \mathbf{K}_1 &= (\bar{2}\bar{3}\bar{3}), & \boldsymbol{\eta}_1 &= [3\bar{1}\bar{1}], & s_1 &= 0.3536, \\ \mathbf{K}_2 &= (\bar{2}11), & \boldsymbol{\eta}_2 &= [111], & s_2 &= 0.3536. \end{aligned} \quad (8)$$

Indeed, the  $\{332\}$  twin is characterized by a misorientation of  $51.1^\circ$  degrees across  $\langle 1\bar{1}0 \rangle$ , consistent with the observation in the twin–twin interaction in Fig. 7a.

Next, we will examine the remarkable twin–twin interaction in the fcc case, where the two distinct twin variants coalesce into a single bcc phase. From the MD simulations in Fig. 4, we monitor the evolution of three orthogonal directions throughout the twin formation process, as visualized in Fig. 8. This tracking leads us to derive a specific set of orientation relations for bcc1, expressed as follows:

$$\begin{aligned} [100]_{bcc} &\leftrightarrow [100]_{fcc} \leftrightarrow [011]_{bcc1} \\ [011]_{bcc} &\leftrightarrow [010]_{fcc} \leftrightarrow [\bar{1}00]_{bcc1} \\ [0\bar{1}1]_{bcc} &\leftrightarrow [001]_{fcc} \leftrightarrow [011]_{bcc1}. \end{aligned} \quad (9)$$

Accordingly, we define the parent basis as  $\mathbf{G}_1 = a_0 \mathbf{e}_1$ ,  $\mathbf{G}_2 = a_0 (\mathbf{e}_2 + \mathbf{e}_3)$ , and  $\mathbf{G}_3 = a_0 (-\mathbf{e}_2 + \mathbf{e}_3)$ , while the twin basis as  $\mathbf{g}_1 = a_0 (\mathbf{e}_2 + \mathbf{e}_3)$ ,  $\mathbf{g}_2 = -a_0 \mathbf{e}_1$ , and  $\mathbf{g}_3 = a_0 (-\mathbf{e}_2 + \mathbf{e}_3)$ . Hence, the correspondence matrix  $C_{ij}$  for this deformation is

$$C_{ij}|_{bcc-fcc-bcc1} = \begin{bmatrix} 0 & -0.5 & -0.5 \\ 1 & 0.5 & -0.5 \\ 1 & -0.5 & 0.5 \end{bmatrix}. \quad (10)$$

For bcc2, the lattice correspondence is found to be

$$\begin{aligned} [100]_{bcc} &\leftrightarrow [100]_{fcc} \leftrightarrow [01\bar{1}]_{bcc2} \\ [011]_{bcc} &\leftrightarrow [010]_{fcc} \leftrightarrow [\bar{1}00]_{bcc2} \\ [0\bar{1}1]_{bcc} &\leftrightarrow [001]_{fcc} \leftrightarrow [011]_{bcc2}, \end{aligned} \quad (11)$$

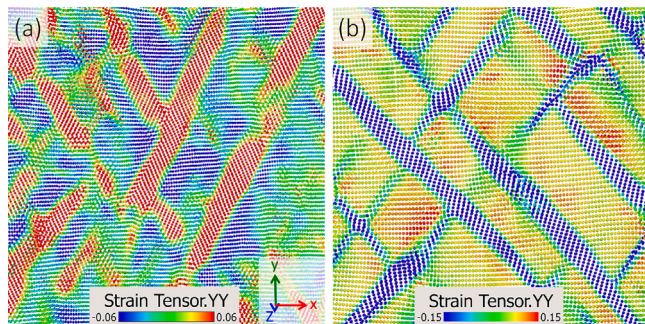


**Fig. 9.** The contour plot displays the strain component  $\epsilon_{yy}$  for (a) the hcp case at a strain of 14.6% and (b) the fcc case at a strain of 15.48%. The red color inside the twins in the hcp case indicates a positive  $\epsilon_{yy}$ , while the blue color inside the twins in the fcc case signifies a negative  $\epsilon_{yy}$ . (For interpretation of the references to color in this figure legend, the reader is referred to the web version of this article.)

leading to a correspondence matrix

$$C_{ij}|_{bcc-fcc-bcc2} = \begin{bmatrix} 0 & -0.5 & -0.5 \\ 1 & -0.5 & 0.5 \\ 1 & -0.5 & 0.5 \end{bmatrix}. \quad (12)$$

When solving the twinning equation for the twin–twin boundary in the fcc case, we are surprised to discover that the stretch  $U$  is identical for both bcc1 (Eq. (10)) and bcc2 (Eq. (12)), so that no solution is found from the twinning equation. In essence, the two co-zone twin variants merge because they have identical stretch  $U$ , preventing the formation of a twin–twin boundary upon their intersection.

In the fcc case, merging bcc1 and bcc2 expedites the rapid growth of these two variants, leading to a substantial portion of merged twins. However, it is crucial to acknowledge that this merging process necessitates the concurrent rotation of bcc1 and bcc2, resulting in pronounced long-range elastic stress. Such high local stress concentration is clearly shown in Fig. S2(a). The earlier merging of bcc1 and bcc2 generates elastic stress that, in turn, hampers the subsequent growth and merging of bcc3 and bcc4. This phenomenon is manifested as localized detwinning of bcc3 and bcc4 in certain regions in Fig. 4d.

#### 3.1.4. Twin mode

While all the twins share the same {112} habit, they involve different intermediate phases and exhibit distinct twin–twin interactions. These disparities necessitate a closer examination of the twinning mode and deformation path for these primary {112} twins. As such, we compare the strain contours for the two cases in Fig. 9. The most prominent observation is the opposing strain component within the twins: the hcp case shows a positive strain component (red in Fig. 9a), while fcc case shows a negative strain component (blue in Fig. 9b). Given that the reference for the strain component is the same – the parent bcc structure – the opposing strain components signify opposite twinning shears between the hcp and fcc cases. Additionally, the magnitude of the strain in the hcp case is one-half of that in the fcc case, as indicated by the color bars in Fig. 9. In other words, the strain contour clearly reveals the distinction between these {112} twins, including their opposing shear directions and different shear magnitudes.

The distinctions observed in the two cases call for additional theoretical calculations to precisely identify the specific twinning modes. Specifically, the stretch tensor components  $U_{ij}$  calculated from the correspondence matrices will be used to determine the exact twinning mode. For the fcc case, based on the correspondence matrix in Eq. (10), we find the following twinning elements

$$\begin{aligned} K_1 &= (21\bar{1}), \quad \eta_1 = [1\bar{1}\bar{1}], \quad s_1 = 0.7071, \\ K_2 &= (\bar{2}1\bar{1}), \quad \eta_2 = [\bar{1}\bar{1}1], \quad s_2 = 0.7071. \end{aligned} \quad (13)$$

It should be noted that for each twin variant, the twinning equation will offer different solutions, even if just a permutation of the

**Table 2**

The summary of the twinning modes observed in each loading condition, along with the corresponding twin–twin interactions.

Loading directions	[100]-compression [011]-tension [0\bar{1}\bar{1}]-tension	[100]-tension [011]-compression [0\bar{1}\bar{1}]-compression
intermediate phase	hcp	fcc
$K_1$ plane	{211}	{211}
$K_2$ plane	{\bar{2}33}	{211}
$\eta_1$ direction	(\bar{1}11)	(1\bar{1}\bar{1})
shear $s$	0.3536	0.7071
twin–twin interaction	{332}\langle 11\bar{3} \rangle	twin merging

same twinning mode. For example, the twinning solutions for the twin variant with the correspondence matrix in Eq. (12) present planes and directions belonging to the same family of Eq. (13),

$$\begin{aligned} K_1 &= (21\bar{1}), \quad \eta_1 = [1\bar{1}\bar{1}], \quad s_1 = 0.7071, \\ K_2 &= (\bar{2}1\bar{1}), \quad \eta_2 = [\bar{1}\bar{1}1], \quad s_2 = 0.7071. \end{aligned} \quad (14)$$

Similarly, based on the correspondence matrix in Eq. (2), we find the following twinning elements for the hcp case

$$\begin{aligned} K_1 &= (\bar{2}\bar{1}\bar{1}), \quad \eta_1 = [1\bar{1}\bar{1}], \quad s_1 = 0.3536, \\ K_2 &= (\bar{2}33), \quad \eta_2 = [311], \quad s_2 = 0.3536. \end{aligned} \quad (15)$$

As summarized in Table 2, twin variants formed through different intermediate phases and, consequently, different deformation paths, exhibit distinct twinning elements. In the fcc case, variant bcc1 has a (211) habit and a shear in [1\bar{1}\bar{1}] direction with a magnitude of 0.7071 ( $\sqrt{2}/2$ ). Conversely, in the hcp case, variant bcc1 maintains the same (211) habit, but an opposite shear in [\bar{1}11] direction with a magnitude of 0.3536 ( $\sqrt{2}/4$ ). In other words, the twinning mode calculation confirms the observation from the MD simulations, showing that the hcp case has an opposite twinning shear direction and half the shear magnitude compared to the fcc case.

Furthermore, based on the twinning elements identified in the equations above, we can readily identify the atomic movements associated with the twin modes within the dichromatic complex. Fig. 10a depicts the {112} twin mode in the fcc case, where all atoms are sheared into their correction positions without undergoing atomic shuffle. It is correlated to the fact that the Bain path for bcc–fcc transformation is a uniform lattice distortion without atomic shuffle. Hence, this twinning mode represents the normal “no shuffle” twin mode observed in numerous bcc structures, including Fe, molybdenum, and tungsten [20, 35].

Contrarily, the {112} twin mode in the hcp case entails both shear and shuffle, as depicted in Fig. 10b. It is again correlated to the fact that the Burgers path for bcc–hcp transformation requires both lattice shear and atomic shuffle. Therefore, this twinning mode corresponds to the “1/2 atoms shuffle” mode, which is the reciprocal of the {332} twin mode (Fig. 10c) widely observed in metastable titanium alloys [9, 10, 67]. From a mathematical perspective, the twinning equation in Eq. (7) has a pair of interchangeable solutions, corresponding to the reciprocal twin pairs of “1/2 atoms shuffle” {112} twin mode and the {332} twin mode. They exhibit identical twinning shear magnitude but interchanged  $K_1$  and  $K_2$  planes, as well as  $\eta_1$  and  $\eta_2$  directions, as evident in their twinning elements in Eqs. (8) and (15).

Moreover, the different twin–twin interactions can also be interpreted by the atomic movements within the twinning modes. Specifically, when different twin variants approach each other, they generate strong elastic interactions that exert substantial local stress. Since the twinning in the fcc case only involves simple shear, the elastic interaction can rotate the twin variants to perfect alignment, resulting in the merging of the impinging twins. In contrast, the twinning in the hcp phase requires both shear and shuffle. Here, the elastic interaction cannot accommodate the “random” atomic shuffle, leading to a problematic state for twin merging. Consequently, a new {332} twin–twin boundary is formed between the impinging twin variants.

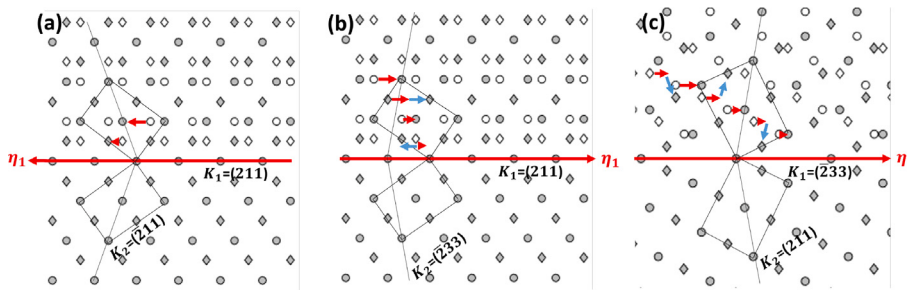


**Fig. 10.** The dichromatic complexes of (a) “no shuffle” {112} twin, (b) “1/2 atoms shuffle” {112} twin, and (c) {332} twins, projected along the  $\langle 1\bar{1}\bar{0} \rangle$  direction. The parent bcc is represented by the bottom gray and top open symbols, while the twin bcc is represented by the top gray symbols. The shear direction  $\eta_1$  and atomic shuffle are shown by red and blue arrows, respectively. (For interpretation of the references to color in this figure legend, the reader is referred to the web version of this article.)

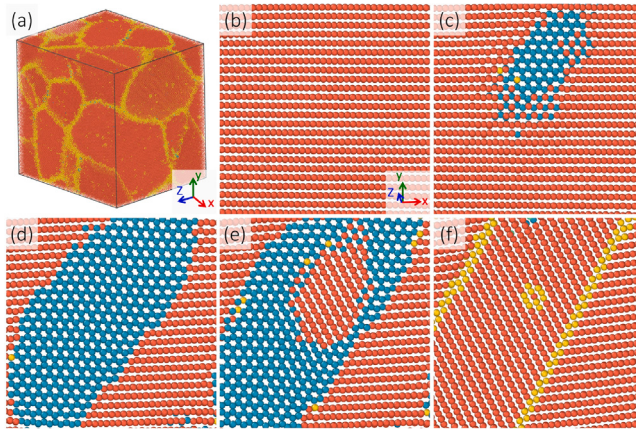


**Fig. 11.** (a) The initial polycrystal Fe is subject to a  $[100]$ -compression at the strain rate of  $10^{10}$  s $^{-1}$  and a temperature of 10 K. (b) A slice of the polycrystal showing a grain in the initial bcc phase. (c) and (d) The nucleation and growth of the intermediate hcp phase. The reverse hcp to bcc phase transformation is initiated in (e) and completed in (f), leading to the formation of {112} twins.

### 3.2. The effect of temperature

The phenomenon of tension–compression asymmetry and the various twinning modes are evident in single crystals. However, investigating the impact of loading direction on polycrystalline structures is intriguing due to the presence of more complex stress and strain conditions. In such cases, additional parameters may play a more pivotal role, such as temperature which is known to introduce twinning asymmetry in hcp materials. Inspired by the hcp and fcc cases observed in Ti alloy, we have chosen Fe as our material of interest for polycrystal. Fe exhibits an hcp structure at low temperatures and transforms to an fcc structure at higher temperatures. Consequently, we will conduct MD simulations to explore deformation in a polycrystalline Fe structure at two significantly different temperatures of 10 K and 800 K.

A meticulous examination and comparison of the microstructure evolution in the two cases allow us to deduce that the {112} twin is formed through an intermediate hcp phase at lower temperatures while involving fcc phases at elevated temperatures. Specifically, in one large grain of Fe polycrystal, we observe the formation of {112} twins through the bcc-hcp-bcc pathway at 10 K (Fig. 11b-f). In contrast, thin layers of fcc atoms are observed during the twin formation in the same grain when the temperature is raised to 800 K (Fig. 12).

It is noted that the random grain orientation of the polycrystal makes it challenging to directly calculate the deformation gradient as in the single crystal case in Section 3.1.2. However, MD simulations offer real-time microstructure evolution, enabling us to identify the conjugate twinning planes and associated twinning modes. Fig. 13 presents the analysis employed to determine the  $K_2$  planes for

the low-temperature case (Fig. 13a-b) and the high-temperature case (Fig. 13c-d).

In Fig. 13a, we trace a  $\{\bar{2}33\}$  plane in the parent phase, which is found to transform into a  $\{233\}$  plane after twinning in Fig. 13b. Thus, the  $K_2$  conjugate twin plane for the {112} twin is determined to be the  $\{233\}$  plane. Based on the theoretical calculation in Section 3.1.4, at low temperatures, the {112} twinning mode is the 1/2 atoms shuffle mode, achieved through the hcp intermediate phase with a smaller shear amount of 0.3536.

In Fig. 13c, we trace a  $\{\bar{2}11\}$  plane in the parent phase, which transforms into another  $\{211\}$  plane after twinning in Fig. 13d. Consequently, at high temperatures, the {112} twinning mode is the no-shuffle mode with a twinning shear amount of 0.7071. As such, the observation in the MD simulations of polycrystalline Fe underscores the significant influence of temperature in altering the twinning mode of the {112} twins. In previous studies, the temperature effect on the deformation in bcc metals and alloys mostly focused on the competition between dislocation slip and deformation twinning. Specifically, with increasing temperature the Peierls barrier for dislocations decreases faster than twinning, leading to the activation of dislocation and the suppression of twinning. Facilitated by the high strain rate in MD simulations, twinning occurs exclusively in the polycrystalline Fe in this work. Such twinning abundance allows us to expand the understanding of temperature effect to the competition between different twinning modes in bcc materials.

### 4. Conclusions

As summarized in Fig. 14, our MD simulations provide valuable insights into the mechanisms that govern the activation of diverse twin modes in bcc materials under distinct loading directions and temperatures. In Ti–Nb single crystal, a tension–compression asymmetry in twinning behavior is observed across all six loading directions. For instance, when loading along  $[100]$ , the {112} twin forms through the bcc-hcp-bcc phase transformation under compression. Conversely, under tension, fcc atomic layers are observed within the twin nuclei. Similarly, our MD simulations of Fe polycrystals reveal the temperature effect on the activation of distinct twin modes. At a low temperature of 10 K, the {112} twin forms via the bcc-hcp-bcc pathway, while increasing the temperature to 800 K leads to the twin formation through the bcc-fcc-bcc pathway.

Though all twins share the same {112} habit plane, the strain contour clearly demonstrates that twins in the two cases have opposing shear directions and different shear magnitudes. The lattice correspondence captured in our MD simulations enables us to determine the complete twinning components. In the fcc case, the twin involves only a shear—in  $[1\bar{1}\bar{1}]$  direction with a magnitude of  $\sqrt{2}/2$ —and represents the normal “no shuffle” twin mode observed in numerous bcc structures. In contrast, in the hcp case, the twin involves an opposite shear in  $[\bar{1}11]$  direction with a magnitude of  $\sqrt{2}/4$ . Notably, this corresponds to the 1/2 atoms shuffle mode, where only half of the atoms are sheared

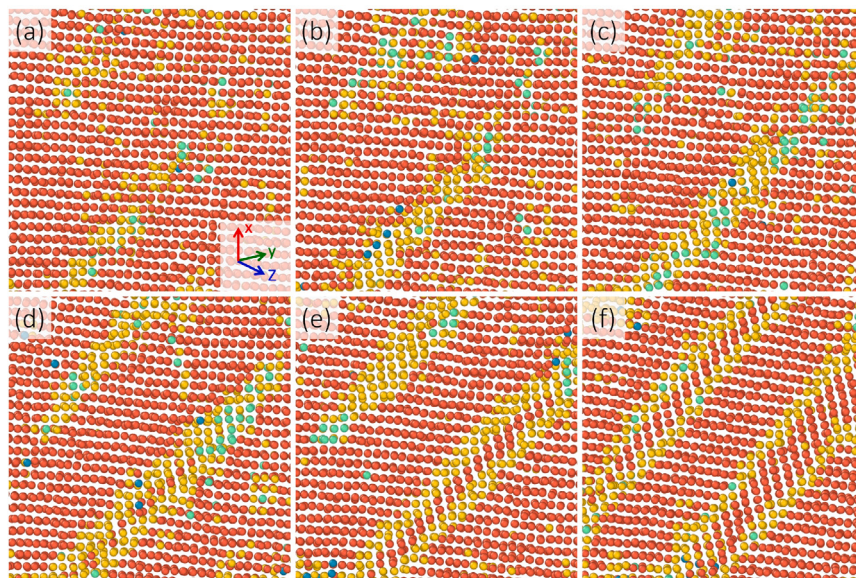


**Fig. 12.** Microstructure evolution in the same grain of the Fe polycrystal under [100]-compression at the strain rate of  $10^{10}$  s $^{-1}$  and a temperature of 800 K. (a-c) With increasing strain, the initial bcc structure begins to form {112} twin nuclei, within which the presence of fcc atoms is evident. (d) and (e) The fcc-bcc reverse phase transformation assists the complete nucleation of {112} twins. (f) The {112} twins continue to grow further.

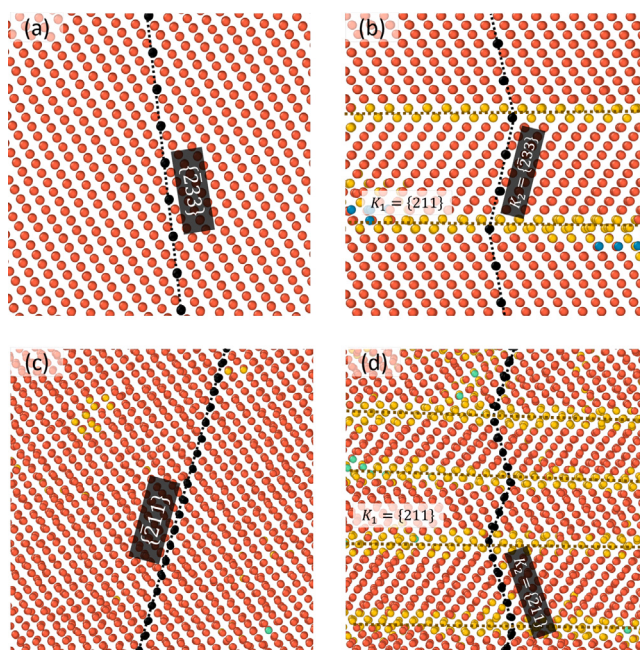


**Fig. 13.** The identification of the conjugate twin plane for the polycrystalline Fe during x-compression. A black plane is tracked during the deformation process to observe its transformation after twinning. The  $K_2$  plane is found to be {233} at 10 K (a-b), while turns into {211} at 800 K (c-d). The microstructure evolution is projected along the  $\langle 1\bar{1}0 \rangle$  direction.

into the correct position, while the other half requires additional atomic shuffle. These intricacies in the twinning modes have significant implications for the twin-twin interactions. The no-shuffle mode in the fcc case facilitates the elastic distortion to align different twin variants, resulting in the merging of twins. However, the shuffle in the hcp case creates a challenging scenario for twin merging, ultimately resulting in the formation of a twin-twin boundary with a {332} habit.

Furthermore, we calculate the deformation gradient and correspondence matrix to investigate the variant selection observed in our MD simulations. The theoretical calculations validate the variant selection

within the MD simulations, confirming not only the number of variants but also the specific variant activated under the mechanical load. These results underscore the pivotal role played by mechanical loading and temperature in the activation of specific twin modes. This insight opens up new opportunities for engineering microstructures through meticulously designed thermomechanical processing techniques [68].

In this work, we focus on unraveling the mechanisms governing loading orientation or temperature-induced twinning mode asymmetry. However, it is worth emphasizing that factors such as loading, temperature, and grain boundaries all directly influence the energy barrier and the minimal energy path for various twinning modes, which ultimately affect twinning modes and variant selection. However, we acknowledge that MD is not the single optimal tool for investigating the coupling and interactions of multiple factors, especially compared to mesoscale approaches such as phase field or crystal plasticity. For example, a comprehensive analysis of the effect of grain boundaries on twinning necessitates the inclusion of many grains in the simulation. This, however, results in substantial, if not formidable, computation costs for MD simulations, which are typically limited to a few million atoms on a regular-sized computing cluster. In contrast, crystal plasticity simulations have the potential to effectively demonstrate the collective influence of grain size and grain misorientation on twin nucleation. Nevertheless, the distinctive advantage of MD simulations lies in their ability to present a well-contained system that isolates a single factor for a rigorous analysis of its impact on twinning behaviors.

#### Declaration of competing interest

The authors declare that they have no known competing financial interests or personal relationships that could have appeared to influence the work reported in this paper.

#### Data availability

The data that support the findings of this study are available from the corresponding author upon reasonable request.

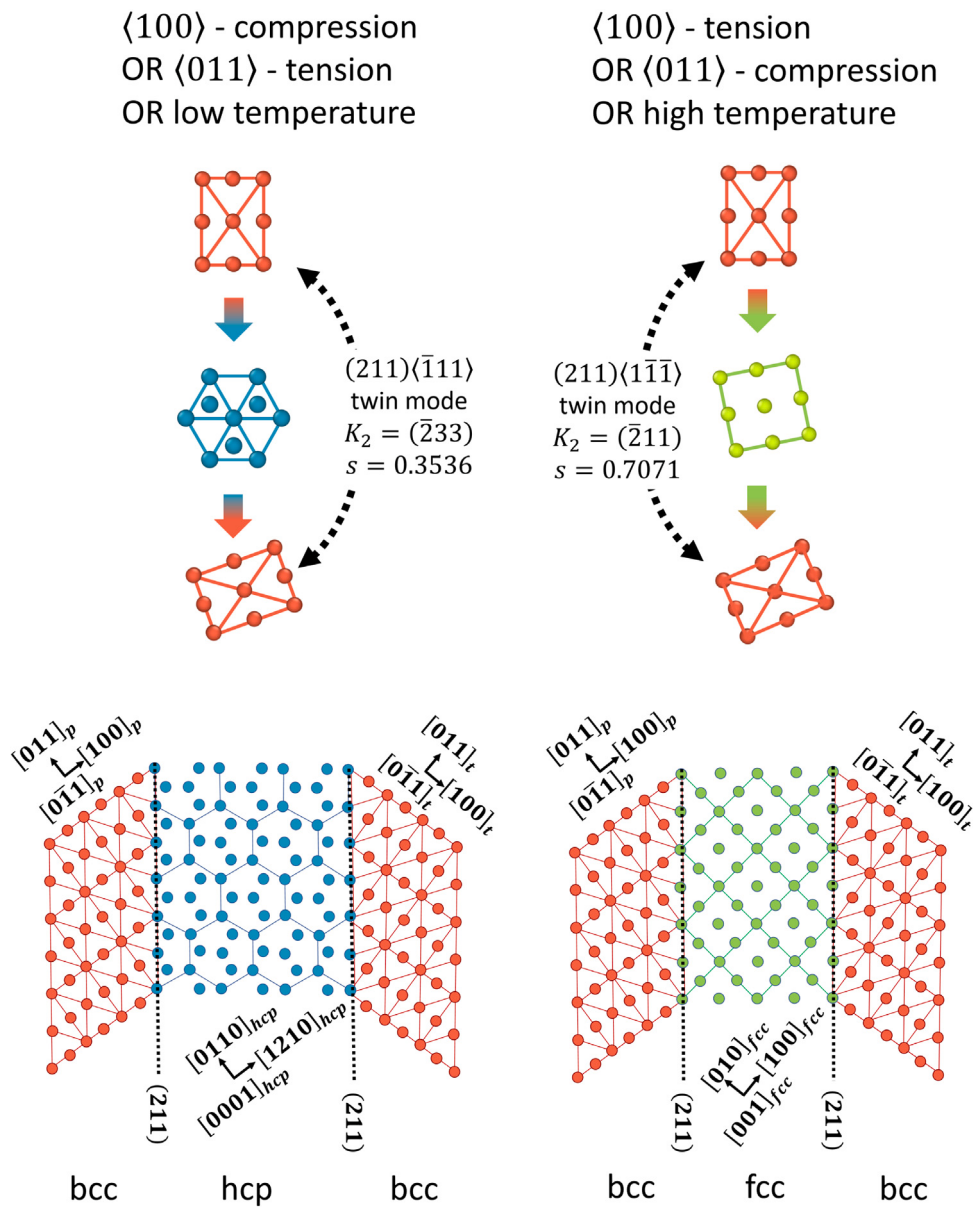


**Fig. 14.** A schematic diagram of the microstructural evolution in bcc structure under different loading or temperature conditions. Left: the case with hcp intermediate phase occurs under [100]-compression or <math>\langle 011 \rangle</math>-tension or low temperature. Right: the case with fcc intermediate phase occurs under [100]-tension or <math>\langle 011 \rangle</math>-compression or high temperature. The bcc, hcp, and fcc atoms are depicted in red, blue, and green colors, respectively. (For interpretation of the references to colour in this figure legend, the reader is referred to the web version of this article.)

## Acknowledgments

The authors acknowledge the financial support from the NSF, USA grant DMR-2240125. The authors also would like to acknowledge the support of Research & Innovation and the Office of Information Technology at the University of Nevada, Reno, for computing time on the Pronghorn High-Performance Computing Cluster.

## Appendix A. Supplementary data

Supplementary material related to this article can be found online at <https://doi.org/10.1016/j.actamat.2024.119681>.

## References

- [1] J. Christian, Some surprising features of the plastic deformation of body-centered cubic metals and alloys, *Metall. Trans. A* 14 (7) (1983) 1237–1256.
- [2] V. Vitek, V. Paidar, Non-planar dislocation cores: A ubiquitous phenomenon affecting mechanical properties of crystalline materials, *Dislocations Solids* 14 (2008) 439–514.
- [3] V. Vitek, R. Perrin, D. Bowen, The core structure of  $1/2\langle 111 \rangle$  screw dislocations in bcc crystals, *Phil. Mag.* 21 (173) (1970) 1049–1073.
- [4] H. Li, S. Wurster, C. Motz, L. Romaner, C. Ambrosch-Draxl, R. Pippan, Dislocation-core symmetry and slip planes in tungsten alloys: Ab initio calculations and microcantilever bending experiments, *Acta Mater.* 60 (2) (2012) 748–758.
- [5] G. Po, Y. Cui, D. Rivera, D. Cereceda, T.D. Swinburne, J. Marian, N. Ghoniem, A phenomenological dislocation mobility law for bcc metals, *Acta Mater.* 119 (2016) 123–135.
- [6] Y. Cui, G. Po, P. Srivastava, K. Jiang, V. Gupta, N. Ghoniem, The role of slow screw dislocations in controlling fast strain avalanche dynamics in body-centered cubic metals, *Int. J. Plasticity* 124 (2020) 117–132.
- [7] P.B. Hirsch, M.J. Whelan, A kinematical theory of diffraction contrast of electron transmission microscope images of dislocations and other defects, *Philos. Trans. R. Soc. London. Ser. A, Math. Phys. Sci.* 252 (1017) (1960) 499–529.
- [8] R. Gröger, A. Bailey, V. Vitek, Multiscale modeling of plastic deformation of molybdenum and tungsten: I. Atomistic studies of the core structure and glide of  $1/2<1\ 1\ 1>$  screw dislocations at 0 k, *Acta Mater.* 56 (19) (2008) 5401–5411.

- [9] J. Xiao, B. He, C. Tan, Effect of martensite on {332} twinning formation in a metastable beta titanium alloy, *J. Alloys Compd.* 895 (2022) 162598.
- [10] X. Zhou, X. a Min, S. Emura, K. Tsuchiya, Accommodative {332}<113> primary and secondary twinning in a slightly deformed  $\beta$ -type Ti-Mo titanium alloy, *Mater. Sci. Eng. A* 684 (2017) 456–465.
- [11] X. Li, Z. Zhang, J. Wang, Deformation twinning in body-centered cubic metals and alloys, *Prog. Mater. Sci.* (2023) 101160.
- [12] J. Wang, Z. Zeng, C.R. Weinberger, Z. Zhang, T. Zhu, S.X. Mao, In situ atomic-scale observation of twinning-dominated deformation in nanoscale body-centred cubic tungsten, *Nature materials* 14 (6) (2015) 594–600.
- [13] S. Wei, Q. Wang, H. Wei, J. Wang, Bending-induced deformation twinning in body-centered cubic tungsten nanowires, *Mater. Res. Lett.* 7 (5) (2019) 210–216.
- [14] Q. Wang, J. Wang, J. Li, Z. Zhang, S.X. Mao, Consecutive crystallographic reorientations and superplasticity in body-centered cubic niobium nanowires, *Sci. Adv.* 4 (7) (2018) eaas8850.
- [15] X. Wang, J. Wang, Y. He, C. Wang, L. Zhong, S.X. Mao, Unstable twin in body-centered cubic tungsten nanocrystals, *Nature Commun.* 11 (1) (2020) 1–7.
- [16] A.H. Zahiri, P. Chakraborty, Y. Wang, L. Cao, Strong strain hardening in ultrafast melt-quenched nanocrystalline Cu: The role of fivefold twins, *J. Appl. Phys.* 126 (7) (2019).
- [17] A.H. Zahiri, J. Ombogo, L. Cao, Formation of {112} 2 contraction twins in titanium through reversible martensitic phase transformation, *Scr. Mater.* 195 (2021) 113694.
- [18] A.H. Zahiri, J. Ombogo, M. Lotfpour, L. Cao, Twinning in hexagonal close-packed materials: The role of phase transformation, *Metals* 13 (3) (2023) 525.
- [19] A. Ostapovets, R. Verma, A. Serra, Unravelling the nucleation and growth of {112} 2 twins, *Scr. Mater.* 215 (2022) 114730.
- [20] Y. Gao, Y. Zhang, Y. Wang, Determination of twinning path from broken symmetry: A revisit to deformation twinning in bcc metals, *Acta Mater.* 196 (2020) 280–294.
- [21] Y. Gao, J.-H. Ke, B. Mao, Y. Liao, Y. Zheng, L.K. Aagesen, Twinning path determined by broken symmetry: A revisit to deformation twinning in hexagonal close-packed titanium and zirconium, *Phys. Rev. Mater.* 4 (7) (2020) 070601.
- [22] A.H. Zahiri, J. Ombogo, T. Ma, P. Chakraborty, L. Cao, Transformation-induced plasticity in omega titanium, *J. Appl. Phys.* 129 (1) (2021).
- [23] H. Tobe, H.Y. Kim, T. Inamura, H. Hosoda, S. Miyazaki, Origin of {3 3 2} twinning in metastable  $\beta$ -Ti alloys, *Acta Mater.* 64 (2014) 345–355.
- [24] R. Wasilewski, On the origin of mechanical twinning—Deformation or transformation? *Metall. Trans. A* 8 (1977) 391–396.
- [25] M. Lai, C.C. Tasan, D. Raabe, On the mechanism of {332} twinning in metastable  $\beta$  titanium alloys, *Acta Mater.* 111 (2016) 173–186.
- [26] P. Castany, Y. Yang, E. Bertrand, T. Gloriant, Reversion of a parent {130}<310>  $\alpha'$  martensitic twinning system at the origin of {332}<113>  $\beta$  twins observed in metastable  $\beta$  titanium alloys, *Phys. Rev. Lett.* 117 (24) (2016) 245501.
- [27] X. Li, Q. Zhao, Y. Tian, Q. Wang, J. Fan, K. Song, H. Zhou, J. Wang, Phase transformation induced transitional twin boundary in body-centered cubic metals, *Acta Mater.* 249 (2023) 118815.
- [28] B. Chen, W. Sun, Omega transitional structure associated with {112}<111> deformation twinning in a metastable beta Ti-Nb alloy, revealed by atomic resolution high-angle annular dark-field scanning transmission electron microscopy, *J. Alloys Compd.* 766 (2018) 123–130.
- [29] Y. Zhu, S. Zhu, J.-F. Nie, Atomic-scale study of {1 1 2} twin boundary structure in a  $\beta$ -Ti alloy, *Phil. Mag. Lett.* 96 (7) (2016) 280–285.
- [30] S. Wu, D. Ping, Y. Yamabe-Mitarai, W. Xiao, Y. Yang, Q. Hu, G. Li, R. Yang, {1 2}<1 1 1> twinning during  $\omega$  to body-centered cubic transition, *Acta Mater.* 62 (2014) 122–128.
- [31] Y. Yang, P. Castany, E. Bertrand, M. Cornen, J. Lin, T. Gloriant, Stress release-induced interfacial twin boundary  $\omega$  phase formation in a  $\beta$  type Ti-based single crystal displaying stress-induced  $\alpha'$  martensitic transformation, *Acta Mater.* 149 (2018) 97–107.
- [32] B. Chen, W. Sun, Transitional structure of {332}<113>  $\beta$  twin boundary in a deformed metastable  $\beta$ -type Ti-Nb-based alloy, revealed by atomic resolution electron microscopy, *Scr. Mater.* 150 (2018) 115–119.
- [33] Y. Yang, H. Zhang, X. Ou, J. Gu, M. Song, Deformation-induced phase transformation and twinning in Fe and Fe-C alloys, *Mater. Sci. Technol.* 37 (15) (2021) 1246–1256.
- [34] A.H. Zahiri, E. Vitral, J. Ombogo, M. Lotfpour, L. Cao, The role of mechanical loading in bcc-hcp phase transition: Tension-compression asymmetry and twin formation, *Acta Mater.* (2022) 118377.
- [35] J.W. Christian, S. Mahajan, Deformation twinning, *Prog. Mater. Sci.* 39 (1–2) (1995) 1–157.
- [36] M.D. Nave, M.R. Barnett, Microstructures and textures of pure magnesium deformed in plane-strain compression, *Scr. Mater.* 51 (9) (2004) 881–885.
- [37] J. Ombogo, A.H. Zahiri, T. Ma, L. Cao, Nucleation of {10 1 2} twins in magnesium through reversible martensitic phase transformation, *Metals* 10 (8) (2020) 1030.
- [38] A. Paxton, Theoretical strength, twinning, antitwinning and pseudotwinning—a quantum-mechanical approach, in: Symposium on Twinning in Advanced Materials, As Part of the 1993 Materials Week, MINERALS, METALS & MATERIALS SOC, 1994, pp. 27–41.
- [39] A. Sleszyk, 1/2 <111> Screw dislocations and the nucleation of {112}<111> twins in the bcc lattice, *Phil. Mag.* 8 (93) (1963) 1467–1486.
- [40] R. Gröger, J. Holzer, T. Kruml, Twinning and antitwinning in body-centered cubic metals, *Comput. Mater. Sci.* 216 (2023) 111874.
- [41] J. Wang, Z. Zeng, M. Wen, Q. Wang, D. Chen, Y. Zhang, P. Wang, H. Wang, Z. Zhang, S.X. Mao, et al., Anti-twinning in nanoscale tungsten, *Sci. Adv.* 6 (23) (2020) eaay2792.
- [42] Z. Li, Y. Cui, Influence of loading orientation on deformation localization of irradiated tungsten, *J. Nucl. Mater.* 573 (2023) 154112.
- [43] A. Akhtar, Compression of zirconium single crystals parallel to the c-axis, *J. Nucl. Mater.* 47 (1) (1973) 79–86.
- [44] M. Knezevic, M. Cezevic, I.J. Beyerlein, J.F. Bingert, R.J. McCabe, Strain rate and temperature effects on the selection of primary and secondary slip and twinning systems in HCP Zr, *Acta Mater.* 88 (2015) 55–73.
- [45] G. Tsukamoto, T. Kunieda, S. Yamasaki, M. Mitsuhashi, H. Nakashima, Effects of temperature and grain size on active twinning systems in commercially pure titanium, *J. Alloys Compd.* 884 (2021) 161154.
- [46] X. Ou, Molecular dynamics simulations of fcc-to-bcc transformation in pure iron: A review, *Mater. Sci. Technol.* 33 (7) (2017) 822–835.
- [47] M. Lai, C.C. Tasan, J. Zhang, B. Grabowski, L. Huang, D. Raabe, Origin of shear induced  $\beta$  to  $\omega$  transition in Ti-Nb-based alloys, *Acta Mater.* 92 (2015) 55–63.
- [48] S. Plimpton, Fast parallel algorithms for short-range molecular dynamics, 1995, pp. 1–19.
- [49] D.J. Evans, B.L. Holian, The Nose-Hoover thermostat, *J. Chem. Phys.* 83 (8) (1985) 4069–4074, <http://dx.doi.org/10.1063/1.449071>.
- [50] M. Parrinello, A. Rahman, Polymorphic transitions in single crystals: A new molecular dynamics method, *J. Appl. Phys.* 52 (12) (1981) 7182–7190.
- [51] A.H. Zahiri, L. Carneiro, J. Ombogo, P. Chakraborty, L. Cao, On the formation of {112} boundary via {1012}–{0112} twin-twin interaction in magnesium, *Comput. Mater. Sci.* 201 (2022) 110887.
- [52] D. Faken, H. Jónsson, Systematic analysis of local atomic structure combined with 3D computer graphics, *Comput. Mater. Sci.* 2 (2) (1994) 279–286.
- [53] J.D. Honeycutt, H.C. Andersen, Molecular dynamics study of melting and freezing of small Lennard-Jones clusters, *J. Phys. Chem.* 91 (19) (1987) 4950–4963.
- [54] A. Stukowski, Visualization and analysis of atomistic simulation data with OVITO—the open visualization tool, *Modelling Simul. Mater. Sci. Eng.* 18 (1) (2009) 015012, <http://dx.doi.org/10.1088/0965-0393/18/1/015012>.
- [55] J. Zhang, F. Sun, Z. Chen, Y. Yang, B. Shen, J. Li, F. Prima, Strong and ductile beta Ti-18Zr-13Mo alloy with multimodal twinning, *Mater. Res. Lett.* 7 (6) (2019) 251–257.
- [56] S. Antonov, Z. Kloenne, Y. Gao, D. Wang, Q. Feng, Y. Wang, H.L. Fraser, Y. Zheng, Novel deformation twinning system in a cold rolled high-strength metastable- $\beta$  Ti-5Al-5V-5Mo-0.5 Fe alloy, *Materialia* 9 (2020) 100614.
- [57] X. Huang, L. Liu, X. Duan, W. Liao, J. Huang, H. Sun, C. Yu, Atomistic simulation of chemical short-range order in HfNbTaZr high entropy alloy based on a newly-developed interatomic potential, *Mater. Des.* 202 (2021) 109560.
- [58] S.A. Etesami, E. Asadi, Molecular dynamics for near melting temperatures simulations of metals using modified embedded-atom method, *J. Phys. Chem. Solids* 112 (2018) 61–72.
- [59] C. Cayron, The transformation matrices (distortion, orientation, correspondence), their continuous forms and their variants, *Acta Crystallograph. Sec. A: Found. Adv.* 75 (3) (2019) 411–437.
- [60] W.G. Burgers, On the process of transition of the cubic-body-centered modification into the hexagonal-close-packed modification of zirconium, *Physica* 1 (7–12) (1934) 561–586.
- [61] E. Bertrand, P. Castany, I. Péron, T. Gloriant, Twinning system selection in a metastable  $\beta$ -titanium alloy by schmid factor analysis, *Scr. Mater.* 64 (12) (2011) 1110–1113.
- [62] X. Min, K. Tsuzaki, S. Emura, T. Sawaguchi, S. Ii, K. Tsuchiya, {332}<113> Twinning system selection in a  $\beta$ -type Ti-15Mo-5Zr polycrystalline alloy, *Mater. Sci. Eng. A* 579 (2013) 164–169.
- [63] Q. Yu, J. Wang, Y. Jiang, R.J. McCabe, N. Li, C.N. Tomé, Twin-twin interactions in magnesium, *Acta Mater.* 77 (2014) 28–42.
- [64] M. Lentz, R. Coelho, B. Camin, C. Fahrenson, N. Schaefer, S. Selve, T. Link, I. Beyerlein, W. Reimers, In-situ, ex-situ EBSD and (HR-) TEM analyses of primary, secondary and tertiary twin development in an Mg-4 wt% Li alloy, *Mater. Sci. Eng. A* 610 (2014) 54–64.
- [65] J.M. Ball, R.D. James, Fine phase mixtures as minimizers of energy, *Arch. Ration. Mech. Anal.* 100 (1) (1987) 13–52.
- [66] K. Bhattacharya, *Microstructure of Martensite: Why It Forms and how It Gives Rise To the Shape-Memory Effect*, Vol. 2, Oxford University Press, 2003.
- [67] N. Kvashin, A. Ostapovets, N. Anento, A. Serra, On the migration of {3 3 2}<1 1 0> tilt grain boundary in bcc metals and further nucleation of {1 1 2} twin, *Comput. Mater. Sci.* 196 (2021) 110509.
- [68] Y.-n. Cui, Z.-l. Liu, Z.-j. Wang, Z. Zhuang, Mechanical annealing under low-amplitude cyclic loading in micropillars, *J. Mech. Phys. Solids* 89 (2016) 1–15.